Energy Materials

Article

Promoted de-solvation effect and dendrite-free Zn deposition enabled by *in-situ* formed interphase layer for high-performance zinc-ion batteries

Binxin Song[1,2], Qiongqiong Lu[1,3,*] , Xinyu Wang[2], Peixun Xiong[4,*]

[1]Henan Key Laboratory of Advanced Conductor Materials, Institute of Materials, Henan Academy of Sciences, Zhengzhou 450001, Henan, China.
[2]Institute of Materials and Technology, Dalian Maritime University, Dalian 116026, Liaoning, China.
[3]Key Laboratory of Advanced Energy Materials Chemistry (Ministry of Education), Nankai University, Tianjin 300071, China.
[4]Inorganic Chemistry I, Technische Universität Dresden, Dresden 01069, Germany.

*Correspondence to: Dr. Qiongqiong Lu, Henan Key Laboratory of Advanced Conductor Materials, Institute of Materials, Henan Academy of Sciences, 11 Changchun Road, Zhengzhou 450001, Henan, China; Key Laboratory of Advanced Energy Materials Chemistry (Ministry of Education), Nankai University, 94 Weijin Road, Tianjin 300071, China. E-mail: qqlu@hnas.ac.cn;
Dr. Peixun Xiong, Inorganic Chemistry I, Technische Universität Dresden, Bergstrasse 66, Dresden 01069, Germany. E-mail: xiongpeixun@163.com

Abstract

The use of aqueous electrolytes and Zn metal anodes in Zn-based energy storage systems provides several benefits, including competitive energy density, excellent safety, and low cost. However, Zn dendrites growth and slow ion transfer at the electrode/electrolyte interphase reduce the cycle stability and rate capability of the Zn anode. Herein, the V_2O_{5-x} interface layer was rationally and controllably constructed on the Zn surface through *in situ* spontaneous redox reaction between V_2O_5 and the Zn anode. The V_2O_{5-x} interface layer, with an optimized thickness, plays a crucial role in ion screening and de-solvation, leading to a uniform dispersion of Zn^{2+} ions and dendrite-free morphology. Moreover, as Zn^{2+} transports through the V_2O_{5-x} interface layer, the V element in a low-valence state allows the oxygen anions to bind more easily with Zn^{2+}. This interaction enables a fast Zn^{2+} diffusion channel in the interfacial layer. Consequently, symmetric cells with V@Zn anodes achieve stable plating/stripping for more than 1,400 h at 1 mA cm^{-2}. In particular, the full cell paired with a V_2O_5 cathode exhibits a capacity of nearly 275.9 mA h g^{-1} at 5 A g^{-1} after 2,500 cycles without obvious capacity deterioration, further highlighting the potential for practical applications.

Keywords: Aqueous Zn-ion batteries, interfacial layer, de-solvation, Zn metal anode

INTRODUCTION

With the large-scale and efficient use of renewable energy such as solar and wind energy, there is an urgent need to develop low-cost, high-safety and high-performance energy storage devices as intermediate media for power transmission[1-3]. Due to the use of aqueous electrolytes, aqueous rechargeable batteries have the benefits of being inexpensive, safe, non-flammable, and environmentally friendly[4-7]. Among them, aqueous Zn-ion batteries (AZIBs) are thought to be a promising kind of rechargeable battery for large-scale applications because of their affordable water electrolyte and manufacturing process, safety, and plentiful Zn resources[8,9]. Unfortunately, the following factors are the principal hindrances to the practical application of Zn metal anodes: growth of Zn dendrites, parasitic reactions, and sluggish transport kinetics[10-12]. Numerous pits on the rough surface of commercial Zn foil result in the unequal distribution of the electric field[13,14]. Zn^{2+} ions preferentially nucleate and deposit inhomogeneously in the convex pits due to the tip effect[15-17]. With repetitive plating/stripping, Zn dendrites develop, resulting in rapid electrolyte consumption and decreased Coulombic efficiency (CE)[18,19]. Furthermore, the dendrites can grow over the separator onto the cathode side, potentially generating an internal short circuit[20-22]. In addition, the chemically active Zn anode reacts with the mild aqueous solution to form the by-product [i.e., $Zn_4SO_4(OH)_6 \cdot nH_2O$], and releases hydrogen (H_2), which leads to rapid capacity decay and cycle instability of AZIBs[23-26].

To address the aforementioned issues, various strategies have been developed to stabilize the Zn anode, including electrolyte modification, structural design, and interface layer construction[27-29]. Among these, the introduction of an interface layer is considered more promising than the other two methods[30-32]. The interface layer not only physically isolates Zn metal from the aqueous electrolyte to inhibit side reactions, but also offers great possibilities for regulating Zn deposition behavior due to its diversity of materials and functions[33-35]. For example, different oxides including ZnO[36], CeO_2[37], WO_3[38], and MoO_3[39] have been used as interfacial materials and have been shown to be effective in Zn anode stabilization. However, it is important to note that most reported interfacial protective layers are quite thick, typically ranging from 5 to 25 μm, to maintain membrane integrity and ensure complete isolation of Zn from the electrolyte [Supplementary Table 1]. For example, Lu *et al.* constructed a 10 μm-thick Layered Double Oxide (LDO) layer to regulate the deposition of Zn[40]. In addition, Zhang *et al.* found that the TiO_2 interface layer with a thickness of 20 μm coupled with optimized plane adjustment could guarantee the uniform deposition of Zn[41]. Considering the poor ion conductivity of these interfacial materials, such a thick coating will inevitably lead to a large internal resistance (R_{ct}) of the battery, resulting in sluggish Zn ion transport kinetics[42,43]. The thin interface layer can alleviate the issue of sluggish transport kinetics, but it may be difficult to resist the drastic volume changes during plating and stripping at high current density[44-46]. In addition, when the interface layer is too thin, it may become nonuniform, which would compromise the effect of Zn metal stabilization[47-49]. Therefore, it is critical to obtain an interface layer with appropriate thickness while minimizing factors that reduce Zn ion transport kinetics[50,51].

Inspired by this, a thin V_2O_{5-x} protective layer was constructed on the surface of the Zn anode by a simple chemical reduction method (designated as V@Zn). By altering the reaction time, the thickness of the protective layer (220 nm, 320 nm, 615 nm) can be precisely controlled. The optimized thickness of the protective layer can prevent direct contact between the electrolyte and Zn metal anode, and demonstrated a de-solvation effect, which effectively promotes the uniform deposition of Zn^{2+} and inhibits dendrite formation. In addition, the low-valent V element in the protective layer promotes the combination of oxygen anion and Zn^{2+}, forming an efficient Zn^{2+} transport channel and accelerating the ion transport process. As a result, the symmetrical V@Zn//V@Zn cell demonstrates an ultra-long life of 1400 h at a current density of 1 mA cm⁻² with a capacity of 1 mA h cm⁻². Moreover, a full cell consisting of a V@Zn

anode and a V_2O_5 cathode shows improved capability and cycling stability.

EXPERIMENTAL
Preparation of V@Zn electrodes
First, 0.6 g of V_2O_5 was added to 50 mL of deionized water. Then, 8 mL of H_2O_2 was poured in and stirred for 30 min. The mixture was introduced to the reactor and heated for 6 h at 190 °C to yield the V_2O_5 solution. After that, a 0.05 mm thick Zn foil with polyimide tape on one side was immersed in the prepared 10 mL of V_2O_5 solution (0.5 mg mL^{-1}) and left for a certain period of time (1, 5, 10 min) to control the thickness of the V_2O_{5-x} layer. Finally, the V@Zn was obtained by rinsing with deionized water and drying overnight in a vacuum oven at 80 °C for 8 h.

X-ray photoelectron spectroscopy (XPS, Perkin Elmer PHI 1600 ESCA) was used to analyze the composition and chemical state of the samples. The microstructure of the specimen was studied using scanning electron microscopy (SEM, SUPRA 55). Elemental analysis of SEM results was obtained using energy dispersive spectrometer (EDS). The wettability of the electrode in the $Zn(CF_3SO_3)_2$ electrolyte was determined using a JC2000C contact angle measurement equipment (POWER EACH, China). Electron paramagnetic resonance (EPR) spectroscopic measurements were performed with a Bruker EMXplus-6/1.

Electrochemical measurements
The CR2032 coin battery was assembled for constant current and CE testing. The CE test was conducted using a charge cut-off voltage of 0.5 V. All tests were performed using Land CT2100A and an electrochemical workstation CHI660E. Symmetrical batteries were assembled using two Zn anodes with a diameter of 1 cm. The half-cell was built with Zn foil as the negative electrode and tested for CE and nucleation overpotential. Zn//Cu and V@Zn//Cu cells were assembled and tested for hydrogen evolution curves at an electrochemical workstation (CHI660E). The V_2O_5 powder was combined with polyvinylidene fluoride (PVDF) and carbon black in N-methyl pyrrolidone (NMP) at a mass ratio of 7:2:1 to create a uniform slurry. The paste is then coated on a stainless-steel mesh and dried in a vacuum oven at 60 °C for 10 h to obtain the cathode. For three-electrode systems, bare Zn or V@Zn is the working electrode and platinum (Pt) foil is the counter-electrode, while Hg/HgCl is the reference electrode. A 3 M $Zn(CF_3SO_3)_2$ aqueous solution was chosen as the electrolyte for the assembly of V@Zn//V_2O_5 full cells. V@Zn, V_2O_5 and filter paper act as anodes, cathodes and separators, respectively. Activation for five cycles at a low current of 1 A g^{-1} before cycling is used. Cyclic voltammetry (CV) and electrochemical impedance spectroscopy (EIS) were tested using the electrochemical workstation (CHI660E). The voltage window of CV was 0.3~1.6 V, and the frequency range of EIS was 100 kHz and 0.01Hz.

RESULTS AND DISCUSSION
The structural and dendritic evolution of the electrode surface following the initial plating and cyclic stages is depicted in the schematic diagram of Figure 1. Due to the uneven deposition of Zn^{2+}, some small protrusions formed on the bare Zn surface. After several cycles, the electron attraction is high at the protrusion due to the tip effect, leading to a large amount of Zn^{2+} deposition[52,53]. After that, the protrusions evolved into Zn dendrites [Figure 1A]. In addition, due to chemical reactions and Zn surface roughness, continuous corrosion begins as soon as the Zn anode comes into contact with the weakly acidic electrolyte. This process consumes both the Zn anode and the electrolyte, producing insulating by-products and hydrogen gas (H_2) [Supplementary Figure 1]. Moreover, the competitive hydrogen evolution reaction (HER) during the recharging process not only directly lowers CE but also accelerates H_2 generation and increases the local pH. These effects lead to elevated internal pressure and intensified parasitic reactions. In contrast, a uniform electric field and homogeneous distribution of Zn^{2+} flux was enabled on the surface
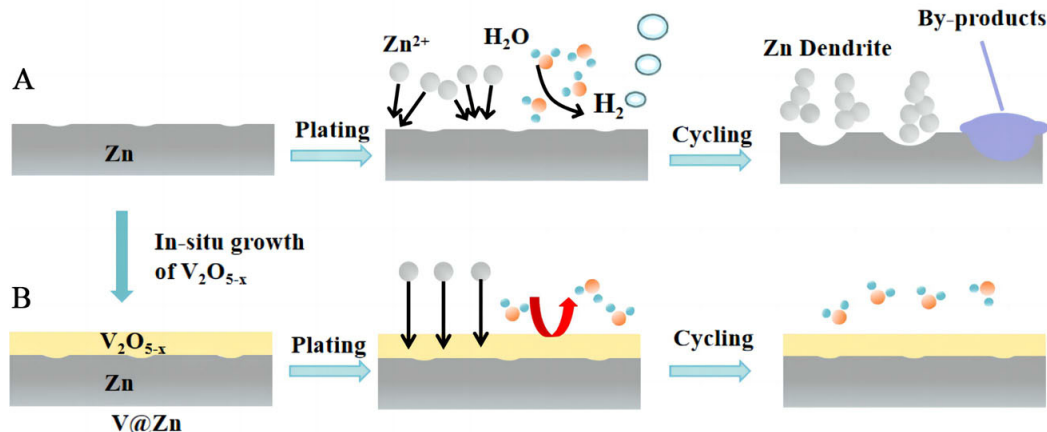
Figure 1. Diagrammatic representation of the surface-structure differences between the (A) bare Zn electrodes and (B) the V@Zn electrodes.

because of the introduction of the V_2O_{5-x} interface interlayer, resulting in uniform deposition of Zn [Figure 1B]. Moreover, the contact between Zn and the electrolyte is effectively blocked, thereby suppressing side reactions.

The V@Zn anode was prepared using a simple *in situ* chemical reduction method [Figure 2A]. The high-valence vanadium oxide in solution is reduced to low-valent vanadium oxide *via* redox reaction with Zn, resulting in the growth of a V_2O_{5-x} layer with yellow color on the surface of bare Zn [Supplementary Figure 2]. The conversion of V_2O_5 to V_2O_{5-x} during assembly can be proved using XPS. The two peaks of the V 2p spectrum in Supplementary Figure 3 show the coexistence of V^{5+} and V^{4+}. V^{5+} is the main valence state of V_2O_5 samples, while the proportion of V^{5+} in V@Zn electrodes decreases. This is attributed to the reduction of V_2O_5 by Zn foil, forming V@Zn. Due to the ultrathin nature of the V2O5-x layer relative to the bare Zn substrate, the X-ray powder diffractio (XRD) patterns of the V@Zn electrodes are dominated by the strong Zn peaks, making them appear similar to those of bare Zn [Supplementary Figure 4]. The XRD pattern of V_2O_{5-x} powder scraped from the V@Zn electrodes aligns well with the standard pattern of $VO_2(H_2O)_{0.5}$ [Supplementary Figure 5]. To further characterize the materials, EPR measurements were also performed. As illustrated in Supplementary Figure 6, V_2O_{5-x} exhibits paramagnetic properties with EPR activity (g=1.96). SEM observation of bare Zn foil and the V@Zn electrode in their original state shows that the surface of bare Zn shows an uneven surface [Figure 2B]. After immersion of Zn in V_2O_5 solution, Zn foil is evenly covered with a porous interface layer [Figure 2C and D, Supplementary Figure 7]. The results from the energy dispersive spectroscopy show a homogeneous distribution of Zn, V, and O elements and the absence of other impurity elements [Figure 2E], demonstrating the uniform V_2O_{5-x} grown on the bare Zn surface.

V@Zn electrodes were obtained by immersing Zn in 0.5 mg mL^{-1} V_2O_5 solution for 1 min, 5 min and 10 min, respectively, named V@Zn-1, V@Zn-5, and V@Zn-10, respectively. By varying the reaction time, the thickness of the V_2O_{5-x} layer can be precisely controlled. SEM results clearly show that the thickness of the layers varies from 220 to 615 nm as the reaction time increases [Figure 3A-C]. As shown in Figure 3D, the polarization voltages of the V_2O_{5-X} layer at 220 nm and 320 nm thickness are lower than those of bare Zn, indicating that V_2O_{5-x} layers promote Zn^{2+} conductivity. However, the polarization voltage of the V_2O_{5-X} layer at 615 nm thickness is significantly higher than that of bare Zn, indicating that the thicker vanadium oxide layer has an inhibitory effect on ion migration. The polarization voltage of plating/stripping increases
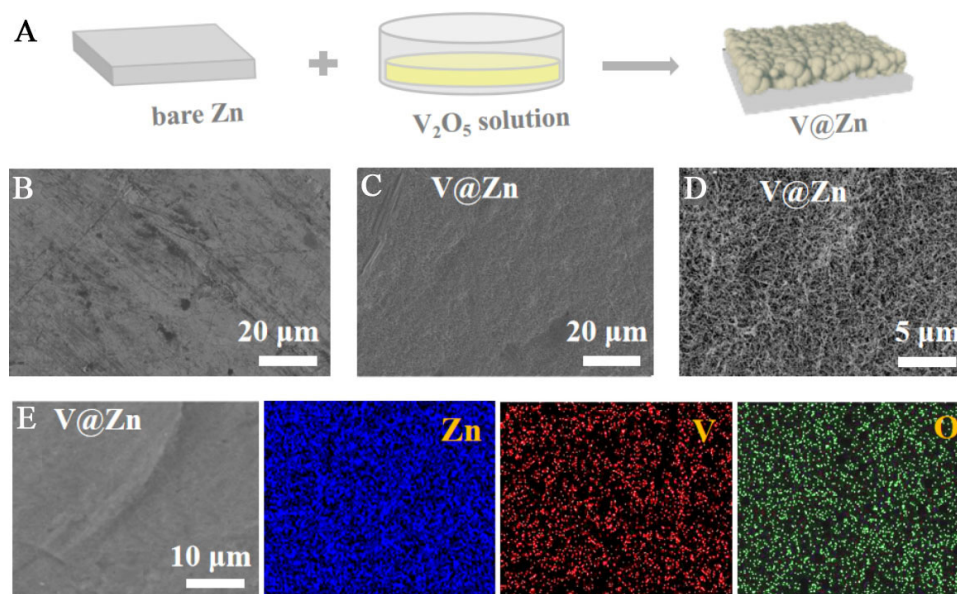
Figure 2. (A) Schematic diagram of V@Zn fabricating; Top-view SEM pictures of the bare Zn foil (B) and V@Zn (C and D); (E) SEM image of V@Zn and corresponding elemental maps. SEM: Scanning electron microscopy.
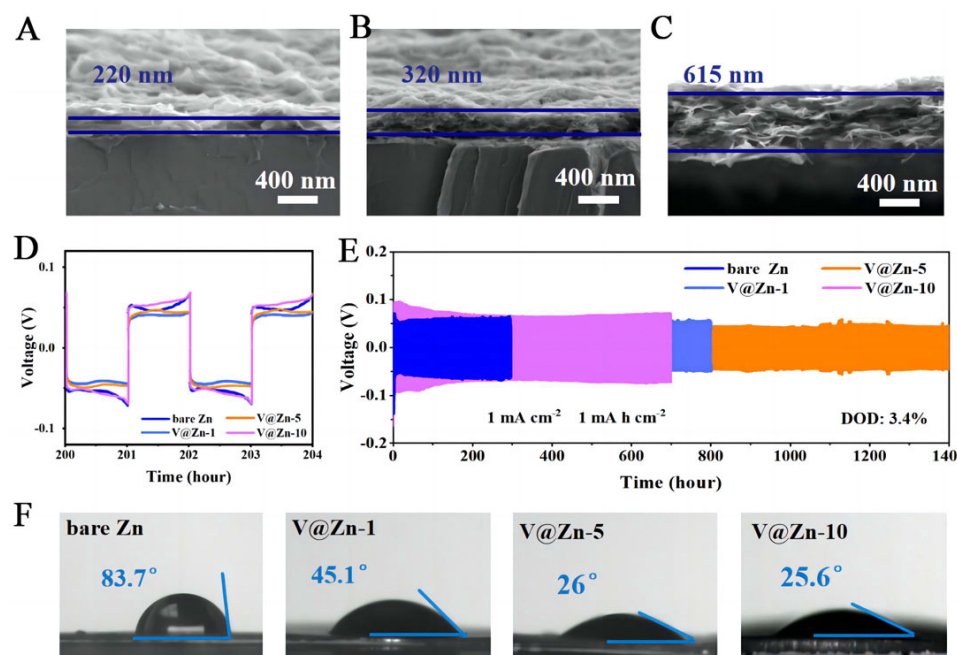

Figure 3. Bare Zn and V_2O_{5-x} protective layer V@Zn after 1, 5 and 10 min reaction, respectively. (A-C) Thickness of the V_2O_{5-x} interface layer; (D) the magnified voltage-time profiles from 200 h to 210 h; (E) long cycle stability testing; (F) contact angle measurement.

with the film thickness, indicating that the film thickness increases the barrier to Zn^{2+} migration. Subsequently, the cycling stability of the V@Zn electrodes and bare Zn was evaluated with symmetrical cells at 1 mA cm^{-2} and 1 mA h cm^{-2}. The sudden drop in voltage at 300 h in bare Zn symmetrical cells is probably due to the formation of dendrites [Figure 3E]. The abrupt failure of the V@Zn-1 symmetrical cell after ~800 h may be due to its weak mechanical strength causing it to fracture during long-term repetitive

plating/stripping. In addition, the V@Zn-10 symmetrical battery only maintains a lifespan of 700 h. This may be due to dendrite formation, which causes a short circuit in the battery. In contrast, a V@Zn-5 symmetrical battery can be stable for more than 1,400 h of cycling, indicating its long-term effectiveness in inhibiting dendrite growth and side reactions.

The compatibility between the electrode surface and the electrolyte was investigated by a contact angle experiment. The contact angles of the 3 M $Zn(CF_3SO_3)_2$ solution with bare Zn and different V@Zn anodes were 83.7°, 45.1°, 26°, and 25.6°, respectively [Figure 3F]. This indicates that the V_2O_{5-x} film improves the wettability of the electrolyte, facilitating Zn-ion transport due to the easy access of the Zn^{2+} in the electrolyte. In summary, the 320 nm-thick V_2O_{5-x} interface layer shows the best stabilization effect and was used for further battery performance evaluation.

In addition to enhancing the plating/stripping kinetics of Zn^{2+}, the V_2O_{5-x} layer is also crucial for adjusting Zn nucleation and enabling uniform Zn deposition. The nucleation overpotential of V@Zn was measured at various current densities in order to demonstrate the function of the V_2O_{5-x} layer in controlling Zn nucleation behavior [Supplementary Figure 8]. Apparently, the nucleation overpotential of the V@Zn at 0.5 mA cm^{-2} is only 20.1 mV, which is even smaller than the 66.1 mV of bare Zn [Supplementary Figure 8A and B]. In addition, this significant difference can still be observed even at higher current densities [Supplementary Figure 8D and E]. This is because when Zn^{2+} passes through the V_2O_{5-x} interface layer, the V element in the protective layer is in a low-valent state, and the oxygen anion in the crystal structure is more likely to bind to Zn^{2+}, so that a Zn^{2+} fast transport channel can be formed. The V_2O_{5-x} layer effectively reduces the nucleation barrier. In addition, it is worth noting that even at the stable Zn deposition stage, the deposition potential of the V@Zn electrode is significantly lower than that of the bare Zn electrode. The V@Zn electrode deposition overpotential (42.2 mV) is significantly less than that of the bare Zn electrode (100.1 mV) at a current density of 0.5 mA cm^{-2}. This pattern is also found at other higher current densities [Supplementary Figure 8C-E].

The current-time curve, as presented in Supplementary Figure 9, shows both the nucleation process and surface variations of the Zn anode[54]. When the -150 mV overpotential is applied, the current of bare Zn continues to decrease for 150 s, showing that the two-dimensional diffusion process is prolonged and Zn deposition remains uncontrolled. During charging and discharging, Zn^{2+} tends to concentrate at the electrode tip, reducing surface energy and speeding dendrite formation on the electrode surface. In contrast, the initial Zn nucleation and two-dimensional diffusion process of the V@Zn reached a stable three-dimensional diffusion after 42 s. Furthermore, the Tafel experiment was conducted to evaluate the corrosion behavior of Zn and V@Zn [Supplementary Figure 10]. Obviously, compared with bare Zn, a V@Zn electrode has a higher corrosion potential, demonstrating that the V_2O_{5-x} protective layer can effectively prevent Zn corrosion by separating Zn from its surrounding electrolyte.

To further investigate cycling performance, symmetrical cells with bare Zn or V@Zn electrodes were built, and charged/discharged tests at various current densities were conducted. Figure 4A and B shows that at a current density of 3 mA cm^{-2}, the symmetrical cell V@Zn//V@Zn has a stable cycle life and voltage distribution over 700 h. On the other hand, the initial polarization voltage of a bare Zn//Zn symmetrical battery is around 55 mV at the start of the cycle, and severe polarization occurs at 120 h. Even at 5 mA cm^{-2} current density, V@Zn//V@Zn cells can sustain nearly 320 h [Figure 4C]. In contrast, Zn//Zn cells undergo a short circuit after 175 h. Different current densities were used to investigate the magnification capabilities of V@Zn and bare Zn [Figure 4D]. At varying current densities, the V@Zn clearly shows lower polarization voltages than bare Zn. Therefore, it was proved that the V_2O_{5-x} layer could lower the polarization voltage of
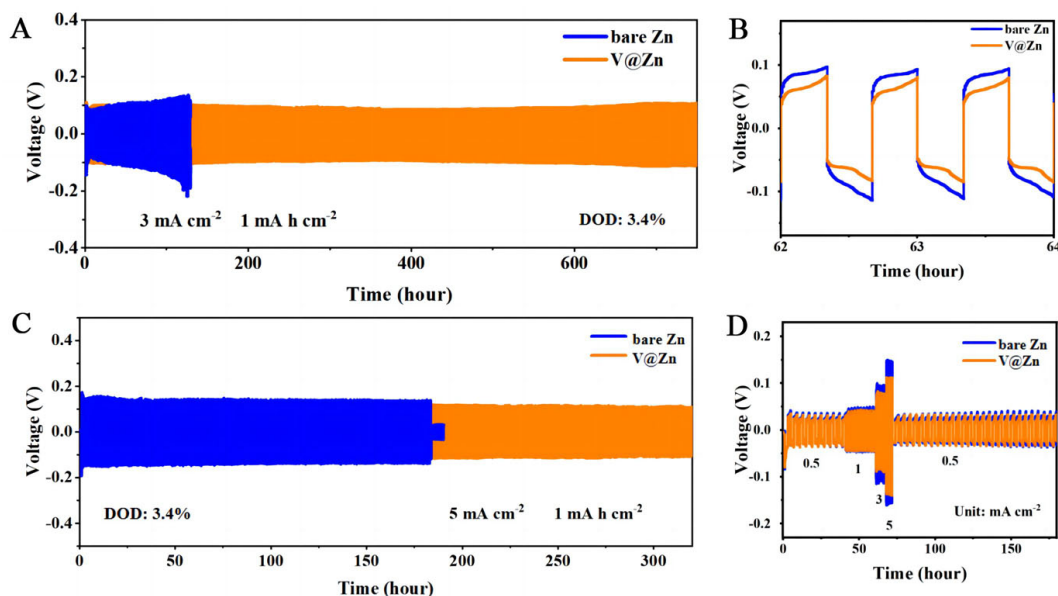
Figure 4. Electrochemical characteristics of symmetric Zn and V@Zn cells. (A) cycling performance at 3 mA cm^{-2}; (B) the magnified graph of the long-cycling voltage profiles, which spans 40 h to 50 h; (C) cycling performance at 5 mA cm^{-2}; (D) rate curves.

the cell and effectively induce uniform Zn^{2+} deposition and inhibit the growth of Zn dendrites[55,56].

In order to further illustrate the effect of V$_2$O$_{5-x}$ layer on the reversibility of Zn plating/stripping, the CE of Zn//Ti asymmetric cells was also studied. As shown in Figure 5A-C, the CE and constant current charge-discharge [galvanostatic charge/discharge (GCD)] curves of a Zn//Ti asymmetric cell with or without a V$_2$O$_{5-x}$ layer are measured at a current density of 3 mA cm^{-2} and 2 mA cm^{-2}. The initial CE of Zn//Ti half-cells is low (79.9%). Zn//Ti has a limited cycle life of 170 cycles, and after 50 cycles, the overpotential of Zn//Ti is as high as 175.8 mV [Figure 5A and B]. In contrast, the V@Zn//Ti half-cell can be stably plated/stripped over 600 cycles, and the overpotential (108.8 mV) is less than that of the bare Zn//Ti cell (175.8 mV) after 50 cycles. At a current density of 2 mA cm^{-2}, the reversibility of plating/stripping of V@Zn//Ti cells is also better than that of bare Zn//Ti cells [Figure 5C]. Furthermore, oxidation/reduction currents in V@Zn//Ti cells are higher than in bare Zn//Ti [Figure 5D]. When the potential negative sweep portion increases, V@Zn//Ti cells (A: -50 mV) are more likely to nucleate than bare Zn//Ti cells (B: -93.2 mV). EIS experiments further verified the kinetic performance of the reaction. Figure 5E and F shows the EIS of bare Zn and V@Zn electrodes at various temperatures between 35 °C and 65 °C. At different temperatures, the R_{ct} of the V@Zn electrode is smaller than that of the bare Zn, which confirms that V$_2$O$_{5-x}$ can increase the charge transfer kinetics. As shown in Figure 5G, the de-solvation activation energy E_a of the V@Zn electrode is about 48.92 kJ mol^{-1}, which is much lower than the 64.84 kJ mol^{-1} of the Zn electrode foil. This indicates that the V$_2$O$_{5-x}$ protective layer can form a fast Zn^{2+} transport channel, which can accelerate the de-solvation process.

In addition, direct evidence of uniform Zn deposition of V$_2$O$_{5-x}$ layers was obtained from *in-situ* optical visualization observations[57,58]. An *in-situ* optical system operating at 5 mA cm^{-2} was utilized to conduct Zn plating tests in order to investigate the effect of the V$_2$O$_{5-x}$-protective technique on dendrite formation. During the plating process, the surface of the V@Zn remains smooth at covered time [Figure 6A]. In contrast, some small protrusions appeared on the surface of bare Zn as early as 15 min, and gradually evolved into Zn dendrites. SEM was used to observe the bare Zn and V@Zn electrodes after 50
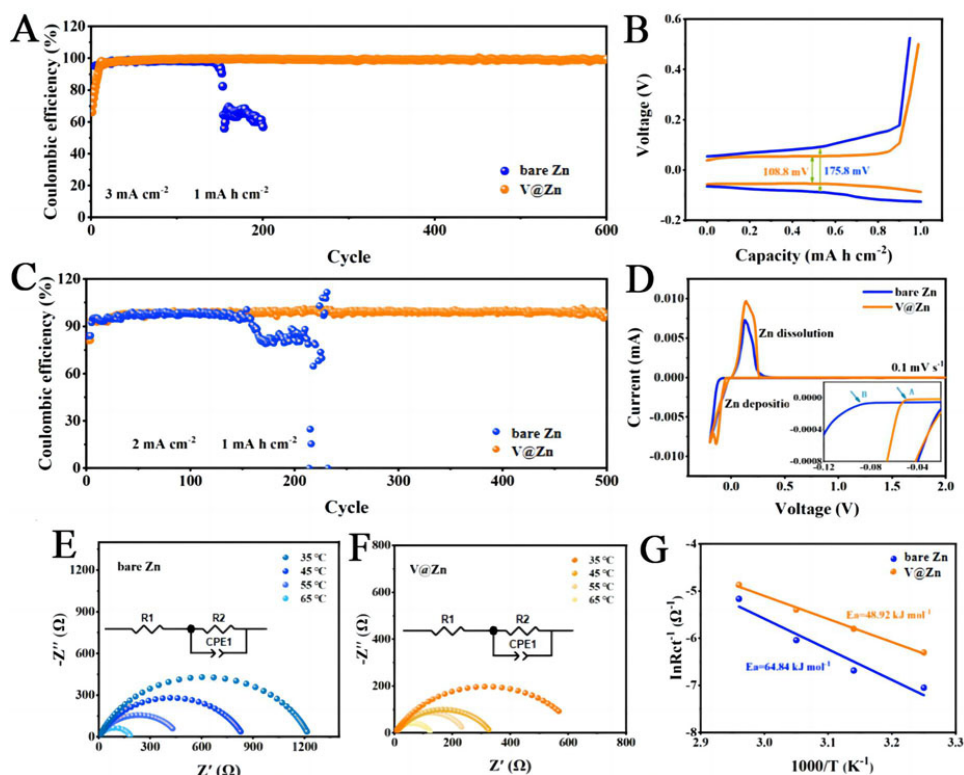
Figure 5. (A) Coulombic Efficiency comparison at 3 mA cm^{-2}; (B) Voltage profiles at the 50th cycle of Zn plating/stripping of V@Zn and bare Zn at 3 mA cm^{-2}; (C) Coulombic Efficiency comparison at 2 mA cm^{-2}; (D) The CV diagram tested at 0.1 mV s^{-1}; EIS of the Zn foil (E) and the V@Zn electrode (F) at different temperatures; (G) The calculated de-solvation activation energies of both electrodes by using the Arrhenius equation. CV: Cyclic voltammetry; EIS: Electrochemical impedance spectroscopy.

plating/stripping cycles. The Zn dendrites of the bare Zn electrode are clearly visible, and the V@Zn electrode is almost horizontal, making the dendrite undetectable [Figure 6B and C]. This indicates that the V_2O_{5-x} protective layer can promote the uniform deposition of Zn^{2+} and prevent dendrite formation. Hydrogen evolution curves were measured for both bare Zn and V@Zn anodes. As shown in Supplementary Figure 11, the V@Zn anode exhibits superior corrosion resistance compared to bare Zn. This improvement can be attributed to the V_2O_{5-x} protective layer coated on the Zn surface, which prevents direct contact between Zn and the electrolyte, thereby suppressing hydrogen evolution. XPS characterizes the changes in the V 2p and Zn 2p of V@Zn during Zn ion plating/stripping [Figure 6D, Supplementary Figure 12]. When Zn^{2+} is intercalated/detached, V^{3+} appears, and the low-valence V can make it easier for the oxygen anion in the crystal structure to bind to Zn^{2+} to form a Zn^{2+} fast transport channel. The position and shape of the Zn 2p peaks on the V@Zn electrode closely align with the peaks of bare Zn. This consistency further confirms the stability of the V_2O_{5-x} layer before and after cycling [Supplementary Figure 13].

The full cell (Zn//V_2O_5 and V@Zn//V_2O_5) was built for electrochemical performance testing to evaluate the effect of the V@Zn anode. The CV curve shows a pair of redox peaks, indicating the insertion/extraction reaction of Zn^{2+} or H$^+$ [Figure 7A]. Furthermore, the gap (0.12 V) between the redox and A1/B1 peaks of V@Zn//V_2O_5 was less than that of the redox peaks of bare Zn//V_2O_5 (0.19 V), indicating that the V_2O_{5-x} interface layer on the Zn anode enables superior electrochemical activity. In addition, EIS testing is also used to verify the reaction kinetics effect of the V_2O_{5-x} layer on the cell. V@Zn//V_2O_5 has a small charge transfer resistance. In Zn//V_2O_5, it is shown that the V_2O_{5-x} coating improves the kinetics of the cell
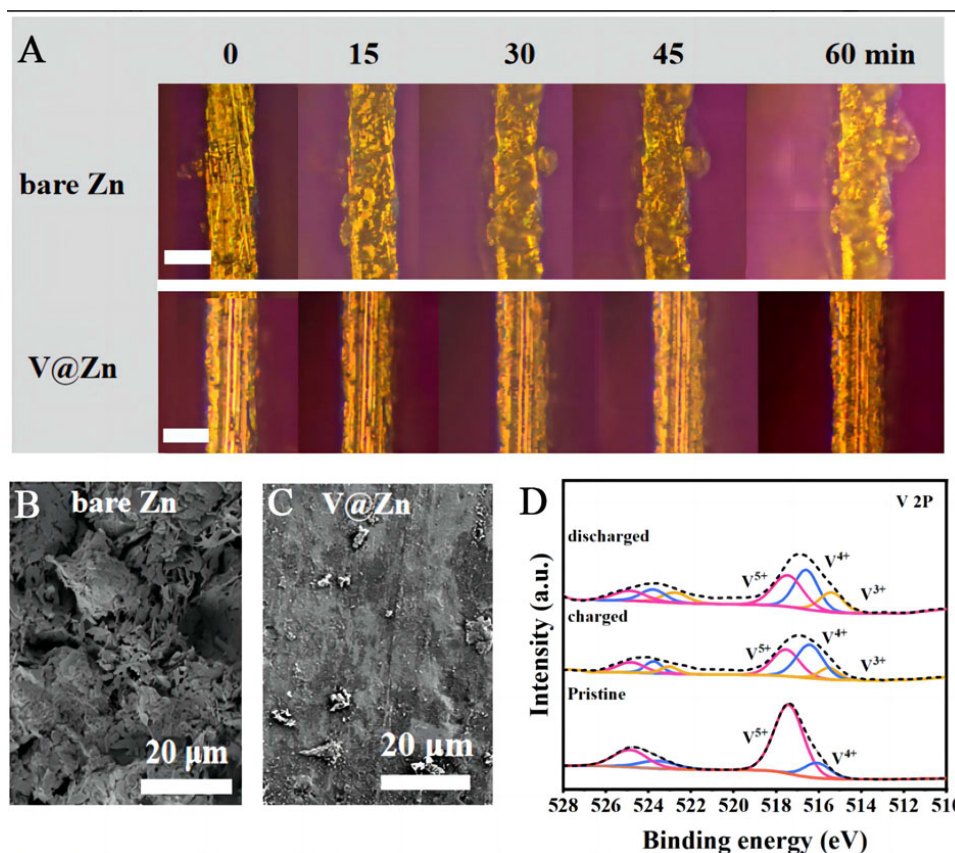
Figure 6. (A) 100 μm scale bar represents light microscopic pictures of Zn deposition on bare Zn and V@Zn surfaces; The SEM pictures of (B) bare Zn and (C) V@Zn after 50 cycles at 1 mA cm^{-2}; (D) V 2p spectra of the V@Zn electrodes in pristine, discharged and charged states. SEM: Scanning electron microscopy.

[Supplementary Figure 14]. The V@Zn//V$_2$O$_5$ battery definitely has a higher rate capability than Zn//V$_2$O$_5$ batteries [Figure 7B]. At a current density of 5 A g^{-1}, V@Zn//V$_2$O$_5$ and Zn//V$_2$O$_5$ cells were tested for long-term cycling. The capacity of Zn//V$_2$O$_5$ batteries is significantly lower than that of V@Zn//V$_2$O$_5$ batteries. In addition, Zn//V$_2$O$_5$ cells experienced significant capacity decay after 1,500 cycles [Figure 7C]. In contrast, V@Zn//V$_2$O$_5$ achieves stable long cycles of more than 2,500 cycles with almost no capacity degradation. In order to make the study more comprehensive, long-term cycling tests were carried out on V@Zn//V$_2$O$_5$ and Zn//V$_2$O$_5$ cells at a current density of 1 A g^{-1}. V@Zn//V$_2$O$_5$ cells maintain high capacity (~340 mA h g^{-1}) over 200 cycles. The capacity of Zn//V$_2$O$_5$ cells is significantly lower than that of V@Zn//V$_2$O$_5$ cells [Supplementary Figure 15]. The findings demonstrate that the V$_2$O$_{5-x}$ coating can effectively prevent dendrite formation, increase corrosion resistance, guide uniform Zn deposition, and promote de-solvation effect, all of which greatly enhance electrochemical performance of zinc-ion batteries.

CONCLUSIONS

A V$_2$O$_{5-x}$ layer is *in situ* grown on the surface of Zn foil by a simple chemical reduction method to guide uniform Zn deposition during plating/stripping process thus preventing the growth of Zn dendrite. In addition, the interface layer can be coordinated with Zn^{2+}, which promotes the de-solvation effect, and can be used as a physical barrier to avoid direct contact between the electrolyte and the Zn anode, reducing the occurrence of side reactions. Therefore, symmetrical cells based on V@Zn anodes exhibit low hysteresis voltage and long cycle life. In addition, the V@Zn//V$_2$O$_5$ full cell shows a capacity of 275.9 mA h g^{-1} after
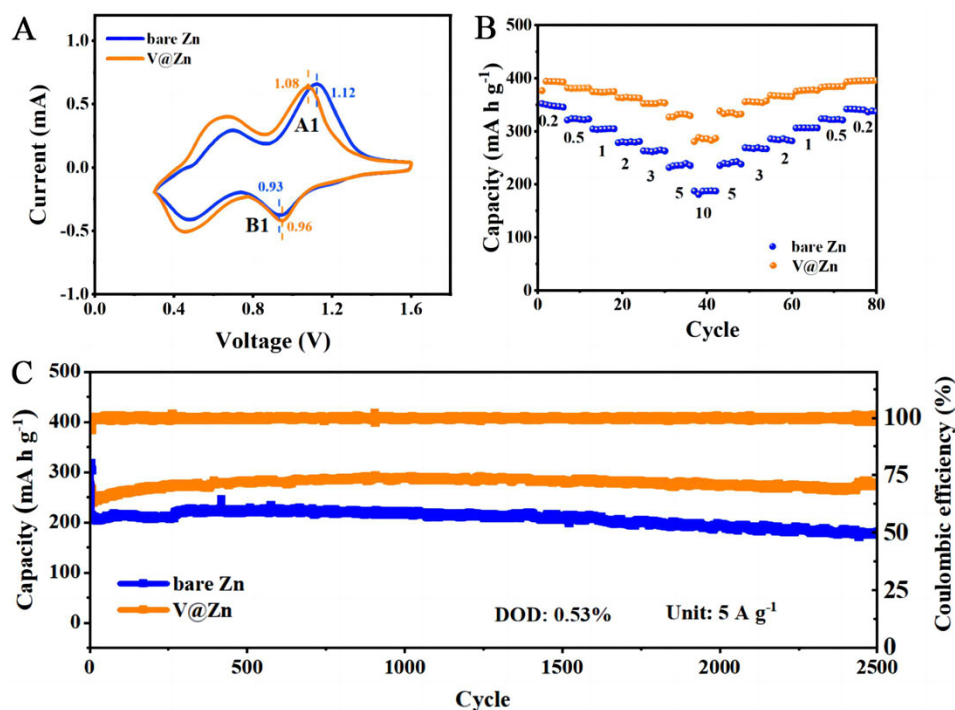
Figure 7. Electrochemical performance of full cells with bare Zn and V@Zn anodes is compared. (A) CV curves at 0.4 mV s^{-1}; (B) Rate performance; (C) Long-term cycling performance at 5 A g^{-1}. CV: Cyclic voltammetry.

2,500 cycles, demonstrating excellent cycling stability. Therefore, this work is expected to open up new avenues for the development of high-performance zinc-ion batteries.

DECLARATIONS

Authors' contributions
Investigation, writing-original draft: Sun, B.
Investigation: Sun, B.; Wang, X.
Supervision, writing - review and editing: Lu, Q.; Wang, X.; Xiong, P.

Availability of data and materials
The data that support the findings of this study are available from the corresponding author upon reasonable request.

Financial support and sponsorship

Conflicts of interest
All authors declared that there are no conflicts of interest.

Ethical approval and consent to participate
Not applicable.

Consent for publication

Not applicable.

Copyright

© The Author(s) 2025.

REFERENCES

1. Xu, Y.; Du, Y.; Chen, H.; et al. Recent advances in rational design for high-performance potassium-ion batteries. *Chem. Soc. Rev.* **2024**, *53*, 7202-98. DOI

2. Yu, L.; Shao, L.; Wang, S.; et al. A low-cost NiSe2 derived from waste nickel foam as a high-performance anode for sodium ion batteries. *Mater. Today. Phys.* **2022**, *22*, 100593. DOI

3. Zhang, X.; Jia, C.; Zhang, J.; Zhang, L.; Liu, X. Smart aqueous zinc ion battery: operation principles and design strategy. *Adv. Sci.* **2024**, *11*, e2305201. DOI PubMed PMC

4. Yang, A.; Yang, C.; Xie, K.; et al. Benchmarking the safety performance of organic electrolytes for rechargeable lithium batteries: a thermochemical perspective. *ACS. Energy. Lett.* **2023**, *8*, 836-43. DOI

5. Wang, H.; Tan, R.; Yang, Z.; Feng, Y.; Duan, X.; Ma, J. Stabilization perspective on metal anodes for aqueous batteries. *Adv. Energy. Mater.* **2021**, *11*, 2000962. DOI

6. Yuan, X.; Wu, X.; Zeng, X.; et al. A fully aqueous hybrid electrolyte rechargeable battery with high voltage and high energy density. *Adv. Energy. Mater.* **2020**, *10*, 2001583. DOI

7. Li, Y.; Ba, H.; Wang, Z.; et al. Electrolyte pH and operating potential: critical factors regulating the anodic oxidation and zinc storage mechanisms in aqueous zinc ion battery. *Mater. Today. Energy.* **2024**, *39*, 101460. DOI

8. Xiao, W.; Yang, S.; Jiang, R.; et al. V_4C_3 MXene-derived $Zn_{0.99}V_5O_{12} \cdot nH_2O$ nanoribbons as advanced cathodes for ultra-long life aqueous zinc-ion batteries. *J. Mater. Chem. A.* **2024**, *12*, 5530-9. DOI

9. Huang, Q.; Shao, L.; Shi, X.; et al. $Na_3V_2O_2(PO_4)_2F$ nanoparticles@reduced graphene oxide: a high-voltage polyanionic cathode with enhanced reaction kinetics for aqueous zinc-ion batteries. *Chem. Eng. J.* **2023**, *468*, 143738. DOI

10. Yuan, L.; Hao, J.; Johannessen, B.; et al. Hybrid working mechanism enables highly reversible Zn electrodes. *eScience* **2023**, *3*, 100096. DOI

11. Wang, Y.; Ren, T.; Wang, Z.; et al. Enabling and boosting preferential epitaxial zinc growth via multi-interface regulation for stable and dendrite-free zinc metal batteries. *Adv. Energy. Mater.* **2024**, *14*, 2400613. DOI

12. Miao, L.; Guo, Z.; Jiao, L. Insights into the design of mildly acidic aqueous electrolytes for improved stability of Zn anode performance in zinc-ion batteries. *Energy. Mater.* **2023**, *3*, 300014. DOI

13. Xu, Y.; Wang, C.; Shi, Y.; Miao, G.; Fu, J.; Huang, Y. A self-preserving pitted texture enables reversible topographic evolution and cycling on Zn metal anodes. *J. Mater. Chem. A.* **2021**, *9*, 25495-501. DOI

14. Fan, W.; Li, P.; Shi, J.; et al. Atomic zincophilic sites regulating microspace electric fields for dendrite-free zinc anode. *Adv. Mater.* **2024**, *36*, e2307219. DOI

15. Li, Y.; Wu, P.; Zhong, W.; et al. A progressive nucleation mechanism enables stable zinc stripping-plating behavior. *Energy. Environ. Sci.* **2021**, *14*, 5563-71. DOI

16. Zhou, M.; Sun, G.; Zang, S. Uniform zinc deposition on O,N-dual functionalized carbon cloth current collector. *J. Energy. Chem.* **2022**, *69*, 76-83. DOI

17. Li, Y.; Li, L.; Zhao, Y.; et al. Homogenizing Zn deposition in hierarchical nanoporous Cu for a high-current, high areal-capacity Zn flow battery. *Small* **2023**, *19*, e2303005. DOI

18. Yu, J.; Yu, W.; Zhang, Z.; Tan, P. Reunderstanding the uneven deposition in aqueous zinc-based batteries. *Chem. Eng. J.* **2024**, *481*, 148556. DOI

19. Zhao, L.; Gao, X.; Gu, Q.; et al. Realizing a dendrite-free metallic-potassium anode using reactive prewetting chemistry. *eScience* **2024**, *4*, 100201. DOI

20. Wang, J.; Ma, Q.; Sun, S.; et al. Highly aligned lithiophilic electrospun nanofiber membrane for the multiscale suppression of Li dendrite growth. *eScience* **2022**, *2*, 655-65. DOI

21. Gonzalez, M. S.; Yan, Q.; Holoubek, J.; et al. Draining over blocking: nano-composite janus separators for mitigating internal shorting of lithium batteries. *Adv. Mater.* **2020**, *32*, e1906836. DOI

22. Zhao, H.; Wan, M.; Zhu, X.; et al. Exploring the disparities in capacity and cycling stability of $NH_4V_4O_{10}$ cathodes in $ZnSO_4$ and $Zn(OTf)_2$ electrolytes. *ACS. Appl. Nano. Mater.* **2024**, *7*, 23712-21. DOI

23. Cao, J.; Zhang, D.; Zhang, X.; Zeng, Z.; Qin, J.; Huang, Y. Strategies of regulating Zn^{2+} solvation structures for dendrite-free and side reaction-suppressed zinc-ion batteries. *Energy. Environ. Sci.* **2022**, *15*, 499-528. DOI

24. Wang, H.; Zhou, A.; Hu, X.; et al. Bifunctional dynamic adaptive interphase reconfiguration for zinc deposition modulation and side reaction suppression in aqueous zinc ion batteries. *ACS. Nano.* **2023**, *17*, 11946-56. DOI

25. Yang, J.; Zhang, Y.; Li, Z.; et al. Three birds with one stone: Tetramethylurea as electrolyte additive for highly reversible Zn-metal anode. *Adv. Funct. Mater.* **2022**, *32*, 2209642. DOI

26. Zhang, Y.; Bi, S.; Niu, Z.; Zhou, W.; Xie, S. Design of Zn anode protection materials for mild aqueous Zn-ion batteries. *Energy. Mater.* **2022**, *2*, 200012. DOI

27. Zhang, Y.; Shi, Y.; Hu, X.; et al. A 3D lithium/carbon fiber anode with sustained electrolyte contact for solid-state batteries. *Adv. Energy. Mater.* **2020**, *10*, 1903325. DOI

28. Hu, Q.; Hu, J.; Li, Y.; et al. Insights into Zn anode surface chemistry for dendrite-free Zn ion batteries. *J. Mater. Chem. A.* **2022**, *10*, 11288-97. DOI

29. Fang, T.; Wu, M.; Lu, F.; Zhou, Z.; Fu, Y.; Shi, Z. Dendrite-free Zn anodes enabled by interface engineering for non-alkaline Zn-air and Zn-ion batteries. *Energy. Mater.* **2024**, *4*, 400039. DOI

30. Ying, H.; Huang, P.; Zhang, Z.; et al. Freestanding and flexible interfacial layer enables bottom-up Zn deposition toward dendrite-free aqueous Zn-ion batteries. *Nano-Micro. Lett.* **2022**, *14*, 180. DOI PubMed PMC

31. Guo, X.; Lu, J.; Wang, M.; et al. Solid-electrolyte interphase governs zinc ion transfer kinetics in high-rate and stable zinc metal batteries. *Chem* **2024**, *10*, 3607-21. DOI

32. Zeng, X.; Gong, Z.; Wang, C.; Cullen, P. J.; Pei, Z. Vanadium-based cathodes modification via defect engineering: strategies to support the leap from lab to commercialization of aqueous zinc-ion batteries. *Adv. Energy. Mater.* **2024**, *14*, 2401704. DOI

33. Zhang, C.; Chou, S.; Guo, Z.; Dou, S. Beyond lithium-ion batteries. *Adv. Funct. Mater.* **2024**, *34*, 2308001. DOI

34. Liu, M.; Cai, J.; Xu, J.; et al. Crystal plane reconstruction and thin protective coatings formation for superior stable Zn anodes cycling 1300 h. *Small* **2022**, *18*, e2201443. DOI

35. Wang, C.; Zeng, X.; Qu, J.; et al. Salt-tolerance training enabled flexible molten hydrate gel electrolytes for energy-dense and stable zinc storage. *Matter* **2023**, *6*, 3993-4012. DOI

36. Cai, J.; Wang, J.; Yu, X.; Long, Y.; Yang, Z. ZnO quantum dots@covalent organic frameworks for high-performance alkaline zinc-based batteries. *J. Mater. Chem. A.* **2023**, *11*, 25692-702. DOI

37. Li, P.; Ren, J.; Li, C.; et al. MOF-derived defect-rich CeO_2 as ion-selective smart artificial SEI for dendrite-free Zn-ion battery. *Chem. Eng. J.* **2023**, *451*, 138769. DOI

38. Tian, G.; Wang, Q.; Qu, Z.; Yu, H.; Zhang, D.; Wang, Q. Coupling engineering of NH_4^+ pre-intercalation and rich oxygen vacancies in tunnel WO_3 toward fast and stable rocking chair zinc-ion battery. *Small* **2023**, *19*, e2206701. DOI

39. Liu, Y.; Wang, J.; Zeng, Y.; Liu, J.; Liu, X.; Lu, X. Interfacial engineering coupled valence tuning of MoO_3 cathode for high-capacity and high-rate fiber-shaped zinc-ion batteries. *Small* **2020**, *16*, e1907458. DOI

40. Lu, X.; Zhao, C.; Chen, A.; et al. Reducing Zn-ion concentration gradient by SO_4^{2-}-immobilized interface coating for dendrite-free Zn anode. *Chem. Eng. J.* **2023**, *451*, 138772. DOI

41. Zhang, Q.; Luan, J.; Huang, X.; et al. Revealing the role of crystal orientation of protective layers for stable zinc anode. *Nat. Commun.* **2020**, *11*, 3961. DOI PubMed PMC

42. Li, B.; Xue, J.; Han, C.; et al. A hafnium oxide-coated dendrite-free zinc anode for rechargeable aqueous zinc-ion batteries. *J. Colloid. Interface. Sci.* **2021**, *599*, 467-75. DOI

43. Li, S.; Liu, Y.; Zhao, X.; et al. Sandwich-like heterostructures of MoS_2/graphene with enlarged interlayer spacing and enhanced hydrophilicity as high-performance cathodes for aqueous zinc-ion batteries. *Adv. Mater.* **2021**, *33*, e2007480. DOI

44. Tan, T.; Lee, P.; Zettsu, N.; Teshima, K.; Yu, D. Y. Highly stable lithium-ion battery anode with polyimide coating anchored onto micron-size silicon monoxide via self-assembled monolayer. *J. Power. Sources.* **2020**, *453*, 227874. DOI

45. Cheng, Z.; Pan, P.; Jiang, L.; et al. Dual structure engineering of SiO_x-acrylic yarn derived carbon nanofiber based foldable Si anodes for low-cost lithium-ion batteries. *J. Colloid. Interface. Sci.* **2022**, *628*, 530-9. DOI

46. Li, X.; Wang, J.; Han, C.; Zeng, K.; Wu, Z.; Wang, D. Surface engineering of nickel-rich single-crystal layered oxide cathode enables high-capacity and long cycle-life sulfide all-solid-state batteries. *Adv. Powder. Mater.* **2024**, *3*, 100228. DOI

47. Wen, Q.; Fu, H.; Huang, Y.; et al. Constructing defect-free zincophilic organic layer via ultrasonic coating for anticorrosive and dendrite-free zinc anode. *Nano. Energy.* **2023**, *117*, 108810. DOI

48. Chen, X.; Li, W.; Hu, S.; et al. Polyvinyl alcohol coating induced preferred crystallographic orientation in aqueous zinc battery anodes. *Nano. Energy.* **2022**, *98*, 107269. DOI

49. Feng, Z.; Zhang, Y.; Gao, Z.; et al. Construction interlayer structure of hydrated vanadium oxides with tunable P-band center of oxygen towards enhanced aqueous Zn-ion batteries. *Adv. Powder. Mater.* **2024**, *3*, 100167. DOI

50. Chen, Y.; Ma, D.; Shen, S.; et al. New insights into high-rate and super-stable aqueous zinc-ion batteries via the design concept of voltage and solvation environment coordinated control. *Energy. Storage. Mater.* **2023**, *56*, 600-10. DOI

51. Dai, Y.; Lu, R.; Zhang, C.; et al. Zn^{2+}-mediated catalysis for fast-charging aqueous Zn-ion batteries. *Nat. Catal.* **2024**, *7*, 776-84. DOI

52. Wang, S.; Yuan, C.; Chang, N.; et al. Act in contravention: a non-planar coupled electrode design utilizing "tip effect" for ultra-high areal capacity, long cycle life zinc-based batteries. *Sci. Bull.* **2021**, *66*, 889-96. DOI

53. Yang, J.; Yan, H.; Hao, H.; et al. Synergetic modulation on solvation structure and electrode interface enables a highly reversible zinc anode for zinc-iron flow batteries. *ACS. Energy. Lett.* **2022**, *7*, 2331-9. DOI

54. Pu, S. D.; Gong, C.; Tang, Y. T.; et al. Achieving ultrahigh-rate planar and dendrite-free zinc electroplating for aqueous zinc battery anodes. *Adv. Mater.* **2022**, *34*, e2202552. DOI

55. Lamaison, S.; Wakerley, D.; Blanchard, J.; et al. High-current-density CO_2-to-CO electroreduction on Ag-alloyed Zn dendrites at elevated pressure. *Joule* **2020**, *4*, 395-406. DOI

56. Raj, V.; Venturi, V.; Kankanallu, V. R.; Kuiri, B.; Viswanathan, V.; Aetukuri, N. P. B. Direct correlation between void formation and

lithium dendrite growth in solid-state electrolytes with interlayers. *Nat. Mater.* **2022**, *21*, 1050-6. DOI PubMed

57. Cao, J.; Zhang, D.; Gu, C.; et al. Manipulating crystallographic orientation of zinc deposition for dendrite-free zinc ion batteries. *Adv. Energy. Mater.* **2021**, *11*, 2101299. DOI

58. Li, Z.; Shu, Z.; Shen, Z.; et al. Dissolution mechanism for dendrite-free aqueous zinc-ions batteries. *Adv. Energy. Mater.* **2024**, *14*, 2400572. DOI